Accepted Manuscript

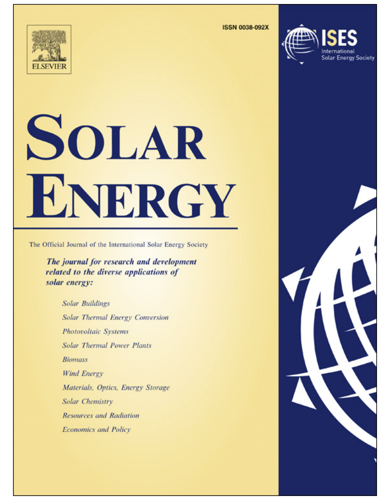

Shadow-band radiometer measurement of diffuse solar irradiance: Calculation of geometrical and total correction factors

Miguel de Simón-Martín, Montserrat Díez-Mediavilla, Cristina Alonso-Tristán

PII: S0038-092X(16)30432-7
DOI: http://dx.doi.org/10.1016/j.solener.2016.09.026
Reference: SE 5355

To appear in: *Solar Energy*

Received Date: 20 June 2016
Revised Date: 21 August 2016
Accepted Date: 21 September 2016

Please cite this article as: de Simón-Martín, M., Díez-Mediavilla, M., Alonso-Tristán, C., Shadow-band radiometer measurement of diffuse solar irradiance: Calculation of geometrical and total correction factors, *Solar Energy* (2016), doi: http://dx.doi.org/10.1016/j.solener.2016.09.026

Shadow-band radiometer measurement of diffuse solar irradiance: calculation of geometrical and total correction factors

Miguel de Simón-Martín[1], Montserrat Díez-Mediavilla, Cristina Alonso-Tristán

Solar and Wind Feasibility Technologies (SWIFT) Research Group, University of Burgos.
Escuela Politécnica Superior (E.P.S.), Campus de Río Vena s/n, 09006, Burgos (Spain).

Abstract

Among the various methods of measuring diffuse solar irradiance, shadowing devices are ones of the most commonly used in solar research all over the world. These instruments work with a basic pyranometer, properly calibrated for the measurement of solar irradiance, with a shadowing element, which can be a disk or a band (Drummond's shadow-band), that prevents the direct incidence of solar beam irradiance on the sensor. This method is capable of precise measurements, but sensor outputs have to be corrected, so as to quantify the amount of diffuse irradiance that the band blocks from reaching the sensor. Several authors have advanced different expressions for this correction factor, most of which only apply to horizontal and equator-oriented tilting pyranometers. In this work, we present a general approach to calculate the geometrical correction factor for a tilted sensor, oriented towards all possible azimuth and zenith angles, which permits the measurement of solar diffuse irradiance on any tilted and oriented surfaces. Furthermore, five total correction models are adapted for measurement in any given direction and evaluated on vertical walls pointing the four cardinal directions. Our results show that geometrical correction improves the Mean Bias Difference (MBD), the Root Mean Squared Difference (RMSD) and the $\mu_{0.99}$ statistics by 60%, 62% and 56%, respectively, in contrast with the raw data. The LeBaron et al. model gives the most accurate figure for total correction according to MBD, RMSD and $\mu_{0.99}$ statistics, with promising average performances of 97%, 91%, and 96%, respectively.

Keywords: Solar diffuse irradiance, shadow-band, instrumentation, correction factor.

1. Introduction

Diffuse solar irradiance is the component of total solar irradiance that is reflected and scattered through the atmosphere. The scattering effects are generated by air molecules and aerosols and are partially dependent on particle density. One portion of total primary and multiple scattered radiation is reflected back to space, another is absorbed, and a third portion reaches the ground (see Fig. 1). The accurate assessment of diffuse irradiance is essential for estimating the incidence of irradiance on different objects such as solar energy collectors and photovoltaic panels. Diffuse irradiance measurements are usually taken from horizontal or tilted planes oriented towards the equator. However, reliable irradiance measurements on planes other than on the horizontal, where it is commonly measured, are necessary to verify solar distribution models, such as those reviewed in (Yang, 2016), applied to buildings equipped with solar collectors (including BIPVs) and sun-tracking devices.

There are several instruments nowadays that allow us to measure solar diffuse irradiance. Drummond's shadow-band, the rotating shadow-band pyranometer, the tracking solar disk and the sky-scanner stand out among others.

Drummond's shadow-band consists of a metal band that blocks the Sun's path in the sky dome (see Fig. 2). The band needs adjustment every few days, depending on the latitude at the mounting place and the day of the year. Due to its simplicity, reduced costs, and ease of operation, it is probably the most extensively used device for the measurement of solar diffuse irradiance.

*Corresponding author at: Department of Electric, Systems and Automatics Engineering. University of León (Spain). Campus de Vegazana s/n, 24071. Tel.: +34 987 29 10 00 5391.

Email addresses: miguel.simon@unileon.es (Miguel de Simón-Martín), mdmr@ubu.es (Montserrat Díez-Mediavilla), catristan@ubu.es (Cristina Alonso-Tristán)

Nomenclature and abbreviations

A_s	Anisotropic coefficient	[-]	s_c	Circumsolar irradiance fraction	[-]
B	Beam direct irradiance	[W·m^{-2}]	V	Transversal observed angle	[rad]
B_{sc}	Solar constant	[W·m^{-2}]	W_{sh}	Shadow-band's width	[m]
D	Diffuse irradiance	[W·m^{-2}]		*Greek symbols*	
D_c	Corrected diffuse measure	[W·m^{-2}]	α	Significance level	[-]
D_{uc}	Uncorrected diffuse measure	[W·m^{-2}]	γ_i	Azimuth angle	[rad]
e_{sh}	Shadow-band thickness	[m]	γ_p	Pyranometer's azimuth angle	[rad]
f_{gc}	Geometrical correction factor	[-]	Δ	Perez et al.'s brightness index	[rad]
f_{tc}	Total correction factor	[-]	δ_s	Sun's declination angle	[rad]
G	Global irradiance	[W·m^{-2}]	ε	Perez et al.'s clearness index	[-]
h_s	Solar elevation	[deg]	ε_0	Earth's orbit excentricity	[-]
I_{sky}	Sky radiance	[W·m^{-2}·sr^{-1}]	θ_{sp}	Sun-pyranometer angle	[rad]
I_g	Albedo's radiance	[W·m^{-2}·sr^{-1}]	θ_{zp}	Pyranometer's zenith angle	[rad]
k_d	Diffuse fraction	[-]	θ_{zsh}	Shadow-bands's zenith angle	[rad]
m	Relative optical air mass	[-]	θ_γ	Zenith angle up to the sensor	[rad]
N	Day of the year	[day]	$\mu_{1-\alpha}$	New statistical estimator	[W·m^{-2}]
R^2	Pearson's correlation coefficient	[-]	ξ_c	Circumnsolar angle	[rad]
R_{gr}	Blocked albedo's reflectance	[W·m^{-2}]	ξ_p	Angle with a patch in the sky	[rad]
R_{sh}	Shadow-band's radius	[m]	ξ_{shp}	Angle with the shadow-band	[rad]
MBD	Mean Bias Difference	[W·m^{-2}]	ρ	Ground reflectance	[-]
RMSD	Root Mean Squared Difference	[W·m^{-2}]	ϕ_g	Geographical latitude	[deg. N]
S	Sky dome fraction	[-]	ω_i	Hour angle	[rad]
s	Side length of a U profile	[m]	ω_{sd}	Semi day-light duration	[rad]

Based on this principle, but simultaneously extended to multiple azimuth and tilting angles, our research group has developed a new device in previous works, called MK6. As it can be seen in Fig. 3, the proposed device (Spanish Patent ES-2562720-B2) is able to measure diffuse solar irradiance directly on four tilted surfaces oriented towards the main cardinal directions: North, South, East and West. A complete description and explanation of its characteristics and operating procedure is presented in (de Simón-Martín et al., 2015).

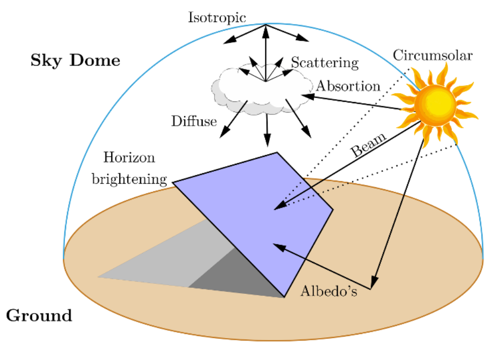

Fig. 1. Solar irradiance components on a tilted surface.

Although this measurement method is accurate and simple, its functional principle relies on blocking solar rays by means of a shadow-band, which means a correction factor is necessary. This correction factor should estimate the correct measurement from the raw data given by the pyranometer analyzing the sky radiance blocked by the shadow-band. Taking into account that a pyranometer measures the solar diffuse irradiance that reaches the Earth's surface on a plane at a solid angle of 2π sr, with the exception of the solid angle blocked by the shadow-band, the geometrical correction factor f_{gc} can be defined as:

$$f_{gc} = \frac{D_c}{D_{uc}} = \frac{2\pi}{2\pi - x} = \frac{1}{1 - \frac{x}{2\pi}} = \frac{1}{1 - S} \qquad (1)$$

where, D_c is the estimation or corrected value of the true diffuse irradiance on the plane, x is the solid angle measured in [sr] blocked by the shadow-band and D_{uc} is the diffuse value registered by the sensor. S is the fraction of the diffuse irradiance intercepted by the shadow-band.

The estimation of diffuse irradiance blocked by the shadow-band may be approached in two main ways:

- Under the hypothesis that the sky radiance is

Fig. 2. Commercial Drummond's shadow-band device. Adapted from (Kipp and Zonen, 2014).

Fig. 3. Multi-directional diffuse solar irradiance measurement device aka MK6. Adapted from (de Simón-Martín et al., 2015).

isotropic and, therefore, homogeneous throughout the sky vault, then all that is needed is a geometrical study of sky radiance projected onto the measuring plane.

- Under the hypothesis that the sky radiance is anisotropic, then (empirical or theoretical) anisotropic models must be applied.

Depending on overcast-sky or clear-sky conditions, either the isotropic or the anisotropic approach will be the most accurate. In general terms, anisotropic models cover a wider range of situations and offer a better performance (Sánchez et al., 2012).

A geometrical (or isotropic) correction was developed by Drummond in 1956 (Drummond, 1956, 1964), while several authors have determined different anisotropic corrections (Sánchez et al., 2013). However, we have noted that these corrections have only been applied to the horizontal and tilted cases oriented towards the Equator (the Equator-oriented case is equivalent to the horizontal case with a corrected geographical latitude: $\phi' = \phi - \theta_{zp}$). In the absence of any indication in methods from international literature that apply either the geometrical correction or the anisotropic models to other surfaces, a generalized geometrical correction model valid for any oriented and tilted surface is presented in this study. Moreover, five acceptably modified anisotropic models (also known as total correction factor models) were evaluated. The most representative correction models in the literature were selected: Batlles et al. (versions A and B) (Batlles et al., 1995; Muneer, 2004; Sánchez et al., 2013), LeBaron (LeBaron et al., 1990), Muneer-Zhang (Muneer and Zhang, 2002) and Steven (Steven and Unsworth, 1980; Steven, 1984).

The paper is organized into six sections. The first describes the methodology and data used in this research work. The characteristics of the validation data and the quality filters are described, including a brief description of the measurement station. In section 3, we extend the generalized geometrical correction factor, introduced in our previous work (de Simón-Martín et al., 2015), including different shadow-band profiles and a parametrical analysis based on the geographical latitude, the azimuth angle and the width-radius ratio. We then describe the total (anisotropic) correction models and their proposed modifications. In section 5, we present the results and discuss the performance of each model according to four statistical estimators. Finally, we present the conclusions in the last section.

2. Materials and methods

A data set of 18 053 measurements, taken every ten minutes on vertical planes oriented toward the four main cardinal points (North, South, East and West), was compared with information from the proposed models, for the purpose of evaluating the correction models under analysis. These data were acquired at a radiometric station installed on the rooftop of the Escuela Politécnica Superior (E.P.S.) of the University of Burgos (42.2122 deg. N, 3.3753 deg. W, 860 m.a.s.l.). The station is operated and maintained by the Solar and Wind Feasibility Technologies Research Group. Obstacles on the horizon are negligible (elevation angles are less than 5 deg.) and top quality standards according to the World Meteorological Organization (WMO) (WMO, 2010) and the National Renewable Energy Laboratory from United States (NREL) (Sengupta et al., 2015) are guaranteed.

The data set included diffuse irradiance measurements on the four previously described planes taken by the MK6 device, which has four sensors (First class pyranometers) and one single multi-lobular shadowband (see Fig. 3). Reference measurements were obtained by the composition model:

$$D_{ref}(\theta_{zp}, \gamma_p) = G(\theta_{zp}, \gamma_p) - B(\theta_{zp}, \gamma_p) - R(\theta_{zp}, \gamma_p), \quad (2)$$

where global irradiance measurements $[G(\theta_{zp}, \gamma_p)]$ were measured by Ph. Schenk 8101 pyranometers (see Fig. 4.a), beam irradiance measurements $[B(\theta_{zp}, \gamma_p)]$ with a Hukseflux DR01 pyrheliometer and ground reflected measurements $[R(\theta_{zp}, \gamma_p)]$ were obtained by a SIR SKS-1110 pyranometer installed in an inverted position. Global and diffuse horizontal irradiances were also measured with Hukseflux SR11 pyranometers mounted on a Geonica SunTracker-3000 (see Fig. 4.b). The sun tracker has a ball that prevents the beam irradiance from reaching the diffuse sensor without obstructing any other sky portion. Thus, the correction factor for these measurements is almost negligible (Ineichen et al., 1983).

The study period encompassed eight months, from September 2014 to April 2015, so as to ensure that a variety of seasonal processes and meteorological conditions were sampled.

All pyranometers were calibrated against a reference pyranometer (Hukseflux SR21) which had in turn been previously calibrated at the World Radiation Center (WRC) in Davos, Switzerland, by using the multiple points calibration method, in order to guarantee measurement quality and comparability. The uncertainties

(a)

(b)

Fig. 4. Main devices from the radiometric station. a) Vertical global irradiance sensors. b) Horizontal global and diffuse sensors and a pyrheliometer mounted on a two-axis sun-tracker.

Table 1. Sensor calculated uncertainties.

Meas.	**Sensor**	**Max. Relative Uncert. [%]**
Glo. North	Ph. Schenk 8101	5.2
Glo. South	Ph. Schenk 8101	5.2
Glo. East	Ph. Schenk 8101	5.2
Glo. West	Ph. Schenk 8101	5.2
Diff. North	Hukseflux SR11	5.6
Diff. South	Hukseflux SR11	5.6
Diff. East	Hukseflux SR11	5.6
Diff. West	Hukseflux SR11	5.6
Glo. Hor.	Hukseflux SR11	4.2
Diff. Hor.	Hukseflux SR11	4.6
Beam	Hukseflux DR01	5.5
Albedo's	SIR SKS-1110	7.8

of all the sensors were calculated by the B method proposed in the (Joint Committee for Guides in Metrology, 2008) and the results are shown in Table 1.

Moreover, the data set under evaluation was subjected to a quality-control procedure, in order to eliminate possible erroneous measurements. The following quality filters proposed in (de Miguel et al., 2001; Muneer, 2004; López et al., 2004; WMO, 2010) were applied to guarantee reliable data:

1. Solar elevation $h_s \geq 5$ deg.
2. $G(0) \geq 0.19$ W·m^{-2}.
3. $G(0) \leq 1.12 B_{sc}$.
4. $B(n) \leq B_{sc}$.
5. $B(n) \geq 0.19$ W·m^{-2}.
6. $B(n)/B_{sc} \leq G(0)/(B_{sc} \cos\theta_{zs}) - 0.5$.
7. $D(0) \leq 1.15 G(0)$.
8. $D(0) \leq 0.8 B_{sc}$.
9. $D(0) \geq 0.19$ W·m^{-2}.
10. $R(180) \geq 0.19$ W·m^{-2}.
11. $R(180) \leq G(0)$.

B_{sc} is the solar constant equal to 1 367 W·m^{-2} according to the WMO.

The models were classified into two groups for the evaluation of their performance:

- Theoretical models: containing certain assumptions regarding the sky-radiance distribution without depending on any empirically-obtained, local parameters.
- Empirical models: containing local coefficients which have to be empirically obtained for the case study, normally through the application of regression techniques to recorded data.

The proposed Generalized Geometrical Correction Model (GGCM) and the Muneer-Zhang Correction Model (MZCM) belong to the group of theoretical models. In contrast, both the Batlles A and B models (BACM and BBCM), the LeBaron model (LBCM) and the Steven model (STCM) are empirical models that need to be adjusted to local coefficients.

A k cross-validation method was implemented to study the performance of the models. So, the whole data set was randomly divided into $k = 10$ subsets of approximately equal size (this implies $\approx$ 1 300 measurement data per set after quality-control filtering). Throughout the $k = 10$ iterations, one subset was the test data set and the combination of the other nine subsets was the training subset. The training subsets were used to adjust the coefficients of the empirical models and the test subset was used to evaluate the performance of the model. The training subset was not used in the case of the theoretical models. The whole procedure was repeated in such a way that every subset was used once for testing. Note that the testing data for each subset was not used in the training of the model and all models were tested with the same subsets, for comparison of the results. The model performance was finally established as the average value over the $k = 10$ iterations obtained by the statistical estimators that were adopted.

Four parameters were considered for the statistical analysis: the Pearson's correlation coefficient (R^2), the Root Mean Squared Difference (RMSD), the Mean Bias Difference (MBD) and the $\mu_{1-\alpha}$-statistic ($\mu_{0.99}$). Their expressions are defined by equations (3), (4), (5) and (6), respectively.

$$R^2 = \frac{\sigma_{XY}^2}{\sigma_X^2 \sigma_Y^2}, \tag{3}$$

$$\mathrm{RMSD} = \sqrt{\frac{1}{N}\sum_{i=1}^{N}\left(D_{c,i} - D_{ref,i}\right)}, \tag{4}$$

$$\mathrm{MBD} = \frac{1}{N}\sum_{i=1}^{N}\left(D_{c,i} - D_{ref,i}\right), \tag{5}$$

$$\mu_{1-\alpha} = \mathrm{sign}(\mathrm{MBD})\left(|\mathrm{MBD}| - t_{\alpha/2}\sqrt{\frac{\mathrm{RMSD}^2 - \mathrm{MBD}^2}{N-1}}\right), \tag{6}$$

where, σ_{XY} is the covariance between X (reference measurements) and Y (corrected values by the model) variables, σ_X is the standard deviation of variable X, σ_Y is the standard deviation of variable Y, $D_{c,i}$ is the ith diffuse corrected value, $D_{ref,i}$ is the ith diffuse reference value, α is the statistical significance (usually taken 0.01) and N is the total number of measurements.

The RMSD value points to the short-term behavior of the model, while the MBD value describes its long-term performance. We should highlight that a few differences of a high magnitude with regard to the reference values will significantly increase the RMSD. Conversely, overestimations can be canceled out by underestimations in the MBD. Moreover, neither the RMSD nor the MBD can provide a confidence interval to give significance to the model's predictions. Thus, in (Stone, 1993), the t-statistic is recommended. It combines both statistical estimators and offers a confidence interval with a statistical significance of α. However, this estimator is based on a very restrictive hypothesis contrast where the mean difference between the estimated and the reference values is assumed to be zero ($\mu = 0$). This estimator was redefined in terms of the value of such a difference, in order to avoid such a limiting restriction, and is now called $\mu_{1-\alpha}$. In this case, we took $\alpha = 0.01$. This estimator includes the sign of the MBD value, in order to analyze whether the proposed model tended either to overestimate (positive sign) or underestimate (negative sign).

For the final decision, 5 rankings (one for each particular direction and one for the overall behavior) including the six models under study were taken into account. The 'all-conditions' ranking was calculated by a non-parametric aggregation procedure, adapted from (Stone, 1994). In this case, the locations were substituted by measured directions.

In all cases, studentized residuals (Moore and McCabe, 2000) were evaluated and absolute values greater than 2 were discarded. Thus, normality, homocedasticity and the independence of the data were found to be acceptable.

Finally, scatter plots for each model and at the four cardinal directions are presented as part of a graphic analysis. Absolute residual diagrams against the horizontal diffuse fraction (k_d) and the angle formed between the sensor and the Sun's position ($\cos\theta_{sp}$) are included. These diagrams were introduced by Ineichen in the mid-1980s (Ineichen et al., 1983) to illustrate an informative representation of a model's performance. Finally, the behavior of each correction model under consideration for all four directions is shown.

3. Generalized geometrical correction (GGCM)

If we consider that the internal reflection in a shadow-band is negligible, the irradiance fraction that it blocks with respect to the total amount of diffuse and albedo irradiance on the sensor can be expressed as:

$$S = \frac{D_r(\theta_{zp},\gamma_p) + R_{gr}(\theta_{zp},\gamma_p)}{D(\theta_{zp},\gamma_p) + R(\theta_{zp},\gamma_p)}, \tag{7}$$

where the index r refers to the shadow-band.

The differential equation of the irradiance incident on the sensor is written as:

$$\frac{dD_r}{d\omega} + \frac{dR_{gr}}{d\omega} = \left(I_{sky} + I_g\right)\cos\theta_{sp} V \cos\delta_s, \tag{8}$$

where V is the transversal angle seen by the sensor, δ_s the Sun's declination angle, and ω the hourly angle. I_{sky} is the sky radiance [W$\cdot$ m^{-2}$\cdot$sr^{-1}], and I_g is the ground reflected radiance [W$\cdot$ m^{-2}$\cdot$sr^{-1}]. If both radiances are supposed to be isotropic, then equations (9) and (10) are verified and we can relate I_{sky} and I_g with the global irradiance on horizontal plane, the diffuse fraction k_d and the ground reflectance ρ.

$$G(0) = \int_0^{2\pi}\int_0^{\pi/2} I_{sky}\cos\theta\sin\theta d\theta d\gamma = \pi I_{sky}. \tag{9}$$

$$I_g = \frac{\rho G(0)}{\pi} = \frac{\rho(D(0)/k_d)}{\pi} = \frac{\rho}{k_d} I_{sky}. \tag{10}$$

By integrating equation (8), taking into account the results of both (9) and (10), the numerator of expression (7) is obtained:

$$\begin{aligned} &D_r(\theta_{zp},\gamma_p) + R_{gr}(\theta_{zp},\gamma_p) \\ &= V I_{sky}\cos\delta_s\left(\int_{\omega_2}^{\omega_3}\cos\theta_{sp}d\omega + \int_{\omega_4}^{\omega_5}\cos\theta_{sp}d\omega\right) \\ &+ \frac{\rho}{k_d} V I_{sky}\cos\delta_s\left(\int_{\omega_1}^{\omega_2}\cos\theta_{sp}d\omega + \int_{\omega_5}^{\omega_6}\cos\theta_{sp}d\omega\right), \end{aligned} \tag{11}$$

where ω_i and $i \in \{1,2,3,4,5,6\}$ are the integral limits according to the zenith and azimuth angles of the inclination and orientation of the pyranometer respectively. Their determination, which constitutes the key to this approach, is explained in depth in subsection 5.

The denominator in expression (7) is obtained by applying the hypothesis of an isotropic distribution of the radiance:

$$\begin{aligned} &D(\theta_{zp},\gamma_p) + R(\theta_{zp},\gamma_p) \\ &= I_{sky}\pi\left(\frac{1+\cos\theta_{zp}}{2} + \frac{\rho}{k_d}\frac{1-\cos\theta_{zp}}{2}\right). \end{aligned} \tag{12}$$

The true value of sky radiance I_{sky} is unnecessary for the calculation of S by the quotient of (11) over (12). Thus, the geometrical correction factor strictly depends on the zenith and azimuth angles of the pyranometer, the transversal observed angle, the spectral reflectance (albedo), and the diffuse fraction.

3.1. Integration limits

The integration limits in equation (11) are the hourly angles measured in the shadow-band's plane, with reference point Q_i and generated by the most restrictive intersection between the shadow-band's plane, the sensor's plane and the horizon plane. An example of these intersections for a sensor characterized by direction $\mathbf{p}$ is shown in Fig. 5.

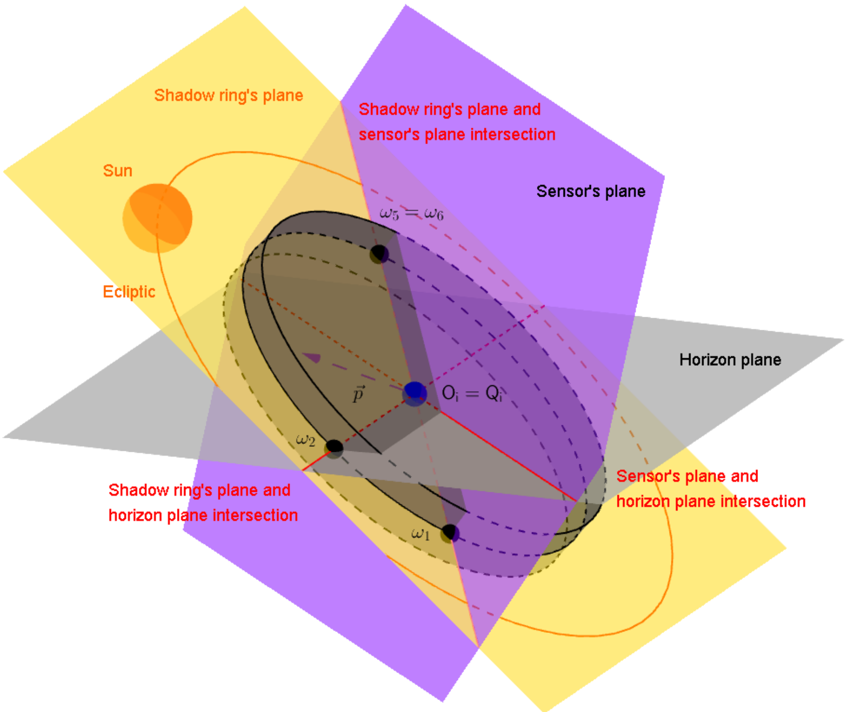

Fig. 5. Plane intersections in the case study.

The intersection between the sensor and the horizon plane can be defined by two hour angles:

$$\omega_{1a} = \arcsin\left(-\frac{\cos\gamma_p}{\cos\delta_s}\right), \tag{13}$$

$$\omega_{2a} = \pi - \arcsin\left(-\frac{\cos\gamma_p}{\cos\delta_s}\right). \tag{14}$$

In the particular case of both the sensor and the horizon are in the same plane, γ_p, the azimuth angle of the pyranometer, can take any value.

The intersection of the shadow-band's plane with the horizon are the sunrise and sunset hour angles, defined by equations (15) and (16).

$$\omega_{1b} = -\omega_{sd} = -|-\tan\phi_g \tan\delta_s|, \tag{15}$$

where ω_{sd} is the hour angle of the semi-daylight duration in [rad] or, in other words, the absolute value of the hour angle between the sunrise and the solar noon.

$$\omega_{2b} = \omega_{sd} = |-\tan\phi_g \tan\delta_s|. \tag{16}$$

At certain geographical latitudes, where $|-\tan\phi_g \tan\delta_s| > 1$, the shadow-band's plane may not intersect with the horizon in certain time periods throughout the year, e.g., in the summer solstice at any region upper the Artic circle. In such cases, if $\tan\phi_g \tan\delta_s < -1$ then $\omega_{sd} = 0$ or if $\tan\phi_g \tan\delta_s > 1$ then it must be assumed that $\omega_{sd} = \pi$.

Finally, the intersection of the planes of both the shadow-band and the sensor can be expressed as:

$$\sin\theta_{zp}\cos\gamma_p R_{sh}\left[\mathrm{sign}(\phi_g)\sin\phi_g\cos\omega - cos\phi_g\tan\delta_s\right] + \sin\theta_{zp}\sin\gamma_p R_{sh}\sin\omega + \mathrm{sign}(\phi_g)\cos\phi_g\cos\omega\cos\theta_{zp}R_{sh} + \sin\phi_g\tan\delta_s\cos\theta_{zp}R_{sh} = 0. \tag{17}$$

If the shadow-band's radius is not null ($R_{sh} \neq 0$) and $\cos\phi_g \neq 0$, then equation (17) can be written as:

$$A\cos\omega + B\sin\omega = C, \tag{18}$$

where, A, B, and C are defined in equations (19), (20), and (21), respectively.

$$A = \tan\phi_g \sin\theta_{zp}\cos\gamma_p + \cos\theta_{zp}. \tag{19}$$

$$B = \frac{\sin\theta_{zp}\sin\gamma_p}{\cos\phi_g}. \tag{20}$$

$$C = \tan\phi_g \tan\delta_s \cos\phi_{zp} + \tan\delta_s \sin\theta_{zp} \cos\phi. \quad (21)$$

Equation (18) can be solved by applying $\lambda = \cos\omega$. Thus, the hour angle limits for the last intersection can be obtained:

$$|\omega_{1c}| = \arccos\left(\frac{AC + B\sqrt{A^2 + B^2 - C^2}}{A^2 + B^2}\right). \quad (22)$$

$$|\omega_{2c}| = \arccos\left(\frac{AC - B\sqrt{A^2 + B^2 - C^2}}{A^2 + B^2}\right). \quad (23)$$

If $A > 0$ and $B > 0$ or $A \geq B$, then the value of ω_{ic}, with $i \in \{1, 2\}$, will be $-|\omega_{ic}|$; otherwise $\omega_{ic} = +|\omega_{ic}|$.

In the case of the sensor plane being parallel to the plane of the shadow-band ($\theta_{zp} = \theta_{zr} = \pi/2 - \phi_g$ and $\gamma_p = -\pi$), both planes do not intersect. So there is no real solution to $A^2 + B^2 - C^2 < 0$ and λ. If $\tan\phi_g \tan\delta_s < 0$, then $\omega_{1c} = \omega_{2c} = 0$, otherwise $\omega_{1c} = -\pi$ and $\omega_{2c} = \pi$.

The integration limits for equation (11) are shown in Table 2 according to the most restrictive hour angles. It should be noted that $\omega_{1a} \leq \omega_{1c}$ and $\omega_{2c} \geq \omega_{2c}$, $\forall \omega_i \in [-\pi, \pi]$.

Table 2. Integration limits for equation (11).

ω_i	$\omega_{1c} \leq \omega_{2c}$	$\omega_{1c} > \omega_{2c}$
ω_1	ω_{1c}	$-\pi$
ω_2	$\max(\omega_{1b}, \omega_{1c})$	$\min(\omega_{2b}, \omega_{2c})$
ω_3	0	ω_{2c}
ω_4	0	ω_{1c}
ω_5	$\min(\omega_{2b}, \omega_{2c})$	$\max(\omega_{1b}, \omega_{1c})$
ω_6	ω_{2c}	π

3.2. Transversal angle and shadow-band geometry

The transversal angle V seen by the pyranometer depends strongly on the shape of the shadow-band's section. We can distinguish two main cases:

I profile: the stretch plate is the most common profile. It consists of a rectangle of negligible thickness ($W_{sh} >> e_{sh}$). The transversal angle V_I observed by the sensor is:

$$V_I = 2\frac{V_I}{2} \approx 2\tan\left(\frac{V_I}{2}\right) \approx 2\frac{\frac{W_{sh}}{2}\cos\delta_s}{\frac{R_{sh}}{\cos\delta_s} + \frac{W_{sh}}{2}\sin\delta_s}, \quad (24)$$

where W_{sh} is the band width and R_{sh} is the average radius of the shadow-band. We can consider that $W_{sh}\sin\delta_s/2$ is negligible in comparison with the other denominator component; then:

$$V_I \approx 2\frac{\frac{W_{sh}}{2}\cos\delta_s}{\frac{R_{sh}}{\cos\delta_s}} = \frac{W_{sh}}{R_{sh}}\cos^2\delta_s. \quad (25)$$

U profile: a blended profile with its aperture on the outside of the band is used by some manufacturers, because it means that the observed transversal angle is independent of the declination angle, if $\tan\delta_s \leq s/W_{sh}$, where s is the side length of the U profile. In this case, the observed transversal angle V_U is:

$$V_U = 2\frac{V_U}{2} \approx 2\sin\left(\frac{V_U}{2}\right) = \frac{\cos\delta_s\sqrt{W_{sh}^2 + s^2}}{R_{sh} + \frac{s}{2}}. \quad (26)$$

Assuming that $s/2$ is negligible in comparison with the shadow-band width, we can simplify the previous equation as follows:

$$V_U \approx \frac{\frac{W_{sh}}{\cos\delta_s}\cos\delta_s}{R_{sh} + \frac{W_{sh}\tan\delta_s}{2}} \approx \frac{W_{sh}}{R_{sh}}. \quad (27)$$

3.3. Parametrical analysis

As demonstrated in the previous section, the geometrical correction factor depends on the geographical latitude, day of the year (declination angle), position of the diffuse sensor (inclination and azimuth angles), the geometrical properties of the shadow-band (width/radius ratio) and the measurement conditions (diffuse fraction and albedo reflectance). Fig. 6 presents the variation of this correction according to some inputs. Subfigures (a), (b) and (c) plot the response surface for the day of the year and the geographical latitude for sensors installed in a vertical position oriented towards the four cardinal points. The last subfigure represents the behavior of this parameter depending on the width/radius ratio for a sensor on an horizontal plane.

It can be observed in this figure that the geometrical correction factor as function of the day of the year is anti-simetrical with respect to the equator (latitude 0 deg.). Furthermore, while the East correction factor matches with the West correction factor, North and

South corrections behave the opposite (when North correction achieves its maximum, South correction gets its minimum, and viceversa). Nevertheless, in all cases it can be observed that the geometrical correction is always greater or equal than zero. Zero correction is obtained when the shadow-band does not intercept the observed sky-dome by the sensor, e.g., a North-facing sensor at the equator in winter. Subfigures (a) and (c) show a disruption at 0 deg. latitude because a North-facing sensor at the North-hemisphere is pointing the pole, while in the South-hemisphere is pointing the equator.

In all subfigures, it can be observed that the f_{gc} behaves in an ondulatory way as a function of the day of the year for a fixed latitude. Because of the evolution of the solar declination angle, it achieves its extreme values at the solstices and the equinoxes, as expected.

Finally, subfigure (d) shows that the greater the W_{sh}/R_{sh} ratio, the greater the disturbance on the observed dome by the sensor is produced and, then, a greater value for the geometrical correction factor is needed.

4. Total correction models

The geometrical correction factor developed in the previous section is based on the hypothesis of evenly distributed radiance throughout the sky dome. This assumption differs from real atmospheric conditions in many cases, specially when clear skies occur. Thus, the proposed correction factor must be modified to include the anisotropic effects in the atmosphere. In this work, the most relevant total correction models in the related literature were analyzed (Muneer, 2004; Sánchez et al., 2012). However, we cannot apply those models directly, but certain modifications are proposed to diffuse measurements on non-horizontal planes.

4.1. Batlles et al. A (BACM)

The first correction model proposed in (Batlles et al., 1995) is based on a multiple linear regression of the geometrical correction factor and on the brightness Δ and the clearness ε indexes proposed in (Perez et al., 1987):

$$f_{tc} = a f_{gc} + b \log \Delta + c \log \varepsilon + d \exp\left(\frac{-1}{\cos\theta_{zs}}\right), \quad (28)$$

where a, b, and c are empirical coefficients obtained from a regression process in a training dataset.

Note that, according to those authors, the expression for ε is:

$$\varepsilon = \frac{D(0) + B(n)}{D(0)}, \quad (29)$$

and is represented in eight intervals, according to the original Perez et al.'s formulation: $(1, 1.056]$, $(1.056, 1.253]$, $(1.253, 1.586]$, $(1.586, 2.134]$, $(2.134, 3.230]$, $(3.230, 5.980]$, $(5.980, 10.080]$ and $(10.080, \infty)$. This formulation differs from (Perez et al., 1990), while expression for Δ remains to be:

$$\Delta = \frac{mD(0)}{B_{sc}\varepsilon_0}, \quad (30)$$

where m is the relative optical air mass and ε_0 the Earth's orbit excentricity.

4.2. Batlles et al. B (BBCM)

The second proposed total correction model is similar to the first one, but it distinguishes only four intervals of ε: $(1, 3.5]$, $(3.5, 8.9]$, $(8.9, 11.0]$ and $(11.0, \infty)$. The generalized expression for this model is:

$$f_{tc} = a_i f_{gc} + b_i \log \Delta + c_i \exp\left(\frac{-1}{\cos\theta_{zs}}\right). \quad (31)$$

For the last two intervals, the c_i coefficient is set to 0. Moreover, although those authors propose general coefficients for each case, these are calculated for horizontal sensor positions. Thus, a particular regression analysis is suggested for greater accuracy. In this case, coefficients have been obtained for vertical sensors oriented towards the cardinal points and the results are shown in Table 3. Coefficient subindexes refer to the clearness index interval.

Table 3. BBCM coefficients for vertical sensors in the four cardinal orientations.

Coeff.	North	South	East	West
a_1	1.1097	0.9141	1.1065	1.0670
b_1	0.0145	0.0762	−0.0084	0.0072
c_1	0.0623	1.0372	−0.3023	0.0144
a_2	1.1470	0.8605	1.0608	1.1136
b_2	0.0070	−0.0466	0.0155	−0.0166
c_2	−0.2464	0.2997	−0.0947	−0.5877
a_3	1.1399	0.7753	1.0441	1.1377
b_3	0.0154	−0.1408	0.0047	0.0708
a_4	1.1463	0.9496	1.1008	1.1579
b_4	0.0400	−0.0299	0.0442	0.0853

4.3. LeBaron (LBCM)

The model described in (LeBaron et al., 1990) correlates corrected values with uncorrected ones, dividing

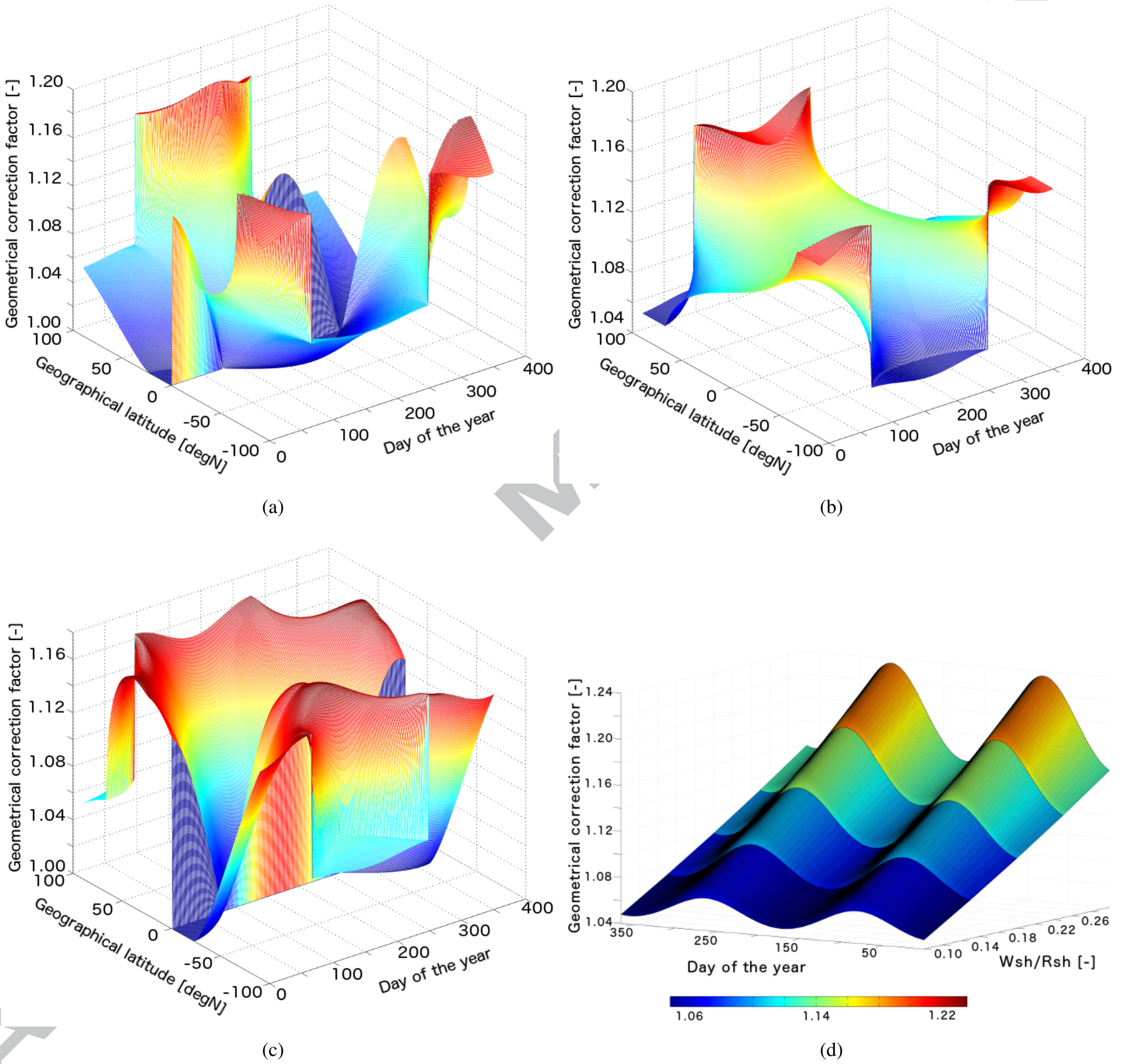

Fig. 6. Parametrical analysis of the geometrical correction factor for sensors tilted 90 degrees, with a U shadow-band (W_{sh}/R_{sh} = 0.15957) and pointing a) North, b) East or West and c) South. d) Geometrical factor dependance with the W_{sh}/R_{sh} ratio for a horizontal sensor. Ground reflectance diffuse fraction have been considered ρ = 0.2 and k_d = 0.5, respectively.

the conditions into four intervals of four estimators according to Table 4. The parameters considered in the model are the Sun's zenith angle, the geometrical correction factor and Perez et al.'s ε and Δ. Thus, in each case study, 256 sub-datasets are generated and a linear regression analysis is performed to obtain the total correction factor. The data sets are not always of a significant size in the training dataset for regression analysis, in which case, the average geometrical correction factor is used.

4.4. Muneer-Zhang (MZCM)

The Muneer-Zhang correction, proposed in (Muneer and Zhang, 2002), is a semi-empirical model based on the radiance distribution index b and the horizontal clearness index k_t. The proposed model follows the expression:

$$f_{tc} = \frac{1}{1 - S'}, \tag{32}$$

where S' is similarly defined to S (see equation (7)), but the irradiance is considered anisotropic rather than isotropic.

The authors divide the sky dome into two quarters: the quarter where the Sun is located (subindex 1) and the opposite one (subindex 2). The radiance distribution index b_i for each quarter depends on k_t according to expressions (33) and (34):

$$b_1 = \begin{cases} \dfrac{3.600 - 10.46k_t}{6.97k_t - 0.400} & \text{if } k_t > 0.2, \\ 1.68 & \text{if } k_t \leq 0.2. \end{cases} \tag{33}$$

$$b_2 = \begin{cases} \dfrac{1.565 - 0.989k_t}{0.66k_t + 0.957} & \text{if } k_t > 0.2, \\ 1.68 & \text{if } k_t \leq 0.2. \end{cases} \tag{34}$$

Thus, the radiance expression for each part of the sky dome can be calculated as:

$$I_{sky,i} = I_z \frac{1 + b_i \cos\theta}{1 + b_i}, \tag{35}$$

where I_z is the zenith radiance which can be calculated from the horizontal diffuse irradiance through equation (36).

$$\frac{D(0)}{I_z} = \int_{-\pi/2}^{\pi/2} \int_0^{\pi/2} \frac{1 + b_1 \cos\theta}{1 + b_1} \cos\theta \sin\theta d\theta d\gamma + \int_{\pi/2}^{3\pi/2} \int_0^{\pi/2} \frac{1 + b_2 \cos\theta}{1 + b_2} \cos\theta \sin\theta d\theta d\gamma. \tag{36}$$

The original model proposed in (Muneer and Zhang, 2002) has been modified for tilted and oriented sensors. The denominator's components of S' can be determined by equations (37) and (38).

$$\begin{aligned} D(\theta_{zp}, \gamma_p) = & \int_{\gamma_1}^{\gamma_2} \int_0^{\pi/2} I_{sky,2} \cos\xi_p \sin\theta d\theta d\gamma \\ & + \int_{\gamma_2}^{\gamma_3} \int_0^{\pi/2} I_{sky,1} \cos\xi_p \sin\theta d\theta d\gamma \\ & + \int_{\gamma_3}^{\gamma_4} \int_0^{\pi/2} I_{sky,2} \cos\xi_p \sin\theta d\theta d\gamma \\ & + \int_{\gamma_1}^{\gamma_2} \int_0^{\theta_\gamma} I_{sky,2} \cos\xi_p \sin\theta d\theta d\gamma \\ & + \int_{\gamma_2}^{\gamma_3} \int_0^{\theta_\gamma} I_{sky,1} \cos\xi_p \sin\theta d\theta d\gamma \\ & + \int_{\gamma_3}^{\gamma_4} \int_0^{\theta_\gamma} I_{sky,2} \cos\xi_p \sin\theta d\theta d\gamma. \end{aligned} \tag{37}$$

$$\begin{aligned} R(\theta_{zp}, \gamma_p) = & \frac{\rho}{k_d} \int_{\gamma_1}^{\gamma_2} \int_{\pi/2}^{\pi-\theta_\gamma} I_{sky,2} \cos\xi_p \sin\theta d\theta d\gamma \\ & + \frac{\rho}{k_d} \int_{\gamma_2}^{\gamma_3} \int_{\pi/2}^{\pi-\theta_\gamma} I_{sky,1} \cos\xi_p \sin\theta d\theta d\gamma \\ & + \frac{\rho}{k_d} \int_{\gamma_3}^{\gamma_4} \int_{\pi/2}^{\pi-\theta_\gamma} I_{sky,2} \cos\xi_p \sin\theta d\theta d\gamma. \end{aligned} \tag{38}$$

In equations (37) and (38), θ_γ is the zenith angle up to the sensor's plane for each azimuth angle γ calculated through equation (39), ξ_p is the angle between a point in the sky dome and the pyranometer's direction and the integration limits γ_i are defined in Table 5.

$$\tan\theta_\gamma = \frac{-\cos\theta_{zp}}{\sin\theta_{zp}\cos\gamma_p\cos\gamma + \sin\theta_{zp}\sin\gamma_p\sin\gamma}. \tag{39}$$

In contrast, the numerator of S' is the sum of diffuse and reflected irradiances intercepted by the shadowband, which can be calculated as a function of the hour angle by expressions (40) and (41).

Table 4. LBCM intervals for input parameters.

Parameter	**Interval 1**	**Interval 2**	**Interval 3**	**Interval 4**
θ_{zs} [deg.]	$[0, 35)$	$[35, 50)$	$[50, 60)$	$[60, 90]$
f_c [-]	$[1.000, 1.068)$	$[1.068, 1.100)$	$[1.100, 1.132)$	$[1.132, \infty)$
ε [-]	$[0.000, 1.253)$	$[1.253, 2.134)$	$[2.134, 5.980)$	$[5.980, \infty)$
Δ [-]	$[0.000, 0.120)$	$[0.120, 0.200)$	$[0.200, 0.300)$	$[0.300, \infty)$

Table 5. Integration limits γ_i for MZCM.

γ_i	$\lvert\gamma_p\rvert \leq \pi/2$	$\lvert\gamma_p\rvert > \pi/2$	$\theta_{zp} = 0$
γ_1	$\gamma_p - \frac{\pi}{2}$	$\lvert\gamma_p\rvert - \frac{\pi}{2}$	$-\pi$
γ_2	$\max(\gamma_p - \frac{\pi}{2}, -\frac{\pi}{2})$	$\max(\lvert\gamma_p\rvert - \frac{\pi}{2}, \frac{\pi}{2})$	$-\frac{\pi}{2}$
γ_3	$\min(\gamma_p + \frac{\pi}{2}, \frac{\pi}{2})$	$\min(\lvert\gamma_p\rvert + \frac{\pi}{2}, \frac{3\pi}{2})$	$+\frac{\pi}{2}$
γ_4	$\gamma_p + \frac{\pi}{2}$	$\lvert\gamma_p\rvert + \frac{\pi}{2}$	$+\pi$

$$
\begin{aligned}
D_{sh}(\theta_{zp}, \gamma_p) = {} & VI_z \cos\delta_s \int_{\omega_4}^{\omega_5} \frac{1 + b_1 \cos\theta_{zsh}}{1 + b_1} \cos\xi_{shp} d\omega \\
& + VI_z \cos\delta_s \int_{\omega_6}^{\omega_7} \frac{1 + b_1 \cos\theta_{zsh}}{1 + b_1} \cos\xi_{shp} d\omega \\
& + VI_z \cos\delta_s \int_{\omega_3}^{\omega_4} \frac{1 + b_2 \cos\theta_{zsh}}{1 + b_2} \cos\xi_{shp} d\omega \\
& + VI_z \cos\delta_s \int_{\omega_7}^{\omega_8} \frac{1 + b_2 \cos\theta_{zsh}}{1 + b_2} \cos\xi_{shp} d\omega. \qquad (40)
\end{aligned}
$$

$$
\begin{aligned}
R_r(\theta_{zp}, \gamma_p) = {} & VI_z \frac{\rho}{k_d} \cos\delta_s \int_{\omega_2}^{\omega_3} \frac{1 + b_1 \cos\theta_{zsh}}{1 + b_1} \cos\xi_{shp} d\omega \\
& + VI_z \frac{\rho}{k_d} \cos\delta_s \int_{\omega_8}^{\omega_9} \frac{1 + b_1 \cos\theta_{zsh}}{1 + b_1} \cos\xi_{shp} d\omega \\
& + VI_z \frac{\rho}{k_d} \cos\delta_s \int_{\omega_1}^{\omega_2} \frac{1 + b_2 \cos\theta_{zsh}}{1 + b_2} \cos\xi_{shp} d\omega \\
& + VI_z \frac{\rho}{k_d} \cos\delta_s \int_{\omega_9}^{\omega_{10}} \frac{1 + b_2 \cos\theta_{zsh}}{1 + b_2} \cos\xi_{shp} d\omega. \qquad (41)
\end{aligned}
$$

θ_{zsh} is the zenith angle of the shadow-band (in [rad]) and ξ_{shp} is the angle between one point of the shadow-band and the pyranometer. The integration limits ω_i are shown in Table 6. The same nomenclature in the definition of the integration limits as in the geometrical correction was used here. Therefore, ω_{1b} and ω_{2b} are the intersections (hour angles) of the shadow-band's plane and the horizon, and ω_{1c} and ω_{2c} are the intersections between the shadow-band and the pyranometer planes.

Integrals from equations (37), (38), (40) and (41) are solved in an analytical way (see Appendix A) through self-programmed MatLab routines, but they can be also solved by applying an adequate numerical integration method implemented in a computation package.

4.5. Steven (STCM)

In (Steven, 1984), a correction model for clear skies is proposed. This model is based on the superimposition of the background isotropic diffuse irradiance and the anisotropic diffuse irradiance from the circumsolar region. So, the fraction S is multiplied by the anisotropic coefficient A_s, completely independent of the geometric correction.

$$f_{tc} = \frac{1}{1 - S A_s}. \qquad (42)$$

The anisotropic coefficient can be calculated as:

$$A_s = 1 - s_c \xi_c + \frac{s_c}{f}, \qquad (43)$$

where s_c is the weighted part of the circumsolar irradiance and ξ_c its observed angle. Both parameters can be estimated by a linear regression from reference values and uncorrected measurements:

$$\frac{D_{ref} - D_{uc}}{S D_{ref}} = \frac{s_c}{f} + (1 - s_c \xi_c). \qquad (44)$$

The parameter f is defined by the author for horizontal pyranometers as one half of the shadow-band length above the horizon, in order to apply the model to any given sensor. The definition of the sensor is modified as follows, in order to apply the model to any given sensor:

$$f = \frac{1}{2} \int_{\omega_2}^{\omega_3} \cos\theta_{sp} d\omega + \frac{1}{2} \int_{\omega_4}^{\omega_5} \cos\theta_{sp} d\omega, \qquad (45)$$

where the integration limits ω_i are obtained from Table 2 and the angle between the Sun and the pyranometer, θ_{sp}, can be calculated by equation (46).

$$\theta_{sp} = \sin\left(\phi_g - \theta_{zp}\right) \sin\delta_s - \cos\left(\phi_g - \theta_{zp}\right) \sin\delta_s. \qquad (46)$$

Table 6. Integration limits ω_i for MZCM.

ω_i	$\omega_{1c} \leq \omega_{2c}$	$\omega_{1c} > \omega_{2c}$
ω_1	ω_{1c}	$-\pi$
ω_2	$\min[\max(\omega_{1c}, -\pi/2), \max(\omega_{1b}, \omega_{1c})]$	$\min[\min(\omega_{2b}, -\pi/2).\omega_{2c}]$
ω_3	$\max(\omega_{1b}, \omega_{1c})$	$\min(\omega_{2b}, \omega_{2c})$
ω_4	$\max[\max(\omega_{1b}, -\pi/2), \omega_{1c}]$	$\max[\min(\omega_{2c}, -\pi/2), \min(\omega_{2b}, \omega_{2c})]$
ω_5	0	ω_{2c}
ω_6	0	ω_{1c}
ω_7	$\min[\min(\omega_{2b}, \pi/2), \omega_{2c}]$	$\min[\max(\omega_{1c}, \pi/2), \max(\omega_{1b}, \omega_{1c})]$
ω_8	$\min(\omega_{2b}, \omega_{2c})$	$\max(\omega_{1b}, \omega_{1c})$
ω_9	$\max[\min(\omega_{2c}, \pi/2), \min(\omega_{2b}, \omega_{2c})]$	$\max[\max(\omega_{1b}, \pi/2), \omega_{1c}]$
ω_{10}	ω_{2c}	π

5. Results and discussion

In Table 7, the results of the correction models described above are shown. A ranking was prepared for all statistical parameters in such a way they are expressed as the value in W·m^{-2}, as percentage of the mean value and rank position. The global ranking was obtained by applying a non-parametric aggregation procedure to the MBD, RMSD, R^2 and $\mu_{0.99}$ results. The value in brackets in the non-parametric aggregation results refers to the significance (α) of the global ranking position. In some cases and for a certain statistical estimator, it could mean that the aggregation of ranking positions of two different models might be the same. In those cases, the performance of both models can not be distinguishable and both models can occupy the same ranking position.

All the correction models improve the results of raw data for all directions except for STCM in relation to the South sensors. The explanation for this result is that the calculation of circumsolar irradiance in STCM is critical for the performance of the model and its uncertainty is magnified, especially for clear-sky conditions. Differences can not be justified by the proposed definition of the f coefficient, because its results in the South direction were the same as those proposed by the author of the model.

Moreover, the results show that the more empirical the model, the better its observed performance. Modeling anisotropy in the sky distribution of solar irradiance is not an easy task, as it involves many factors. The complexity of pure theoretical models for fine corrections may not be worthwhile in the long run.

The results showed that BBCM had the best performance for the North measures, LBCM performed best for the South and West directions and BACM obtained the best results for the East measures.

According to the non-parametric aggregation, LBCM achieved the best ranking position for MSD, RMSD and $\mu_{0.99}$ at a significance level of $\alpha \geq 0.001$. The R^2 results for all the models were very similar and offered no clear classification criteria.

It can also be observed that LBCM underestimates the South direction and tends to overestimate the rest. Nevertheless, according to the $\mu_{0.99}$ estimator, differences are less than 1 W·m^{-2} in all cases.

It must be noticed that the absolute value of MBD and RMSD for the top 3 so ranked correction models can be smaller than the measurement uncertainties. Although the maximum relative uncertainty is obtained for low values of measured irradiance, and it decreases as the measured value increases, models' performances may be undistinguisable under these circumstances. Thus, differences between LBCM, BACM and BBCM can not be done according to those estatistical estimators. $\mu_{0.99}$ results helpful in these cases.

Figure 7 shows the scatter plots for each cardinal direction of all the correction models under consideration. Only the results with studentized residuals lower than 2 have been considered. Most models behave acceptably for diffuse irradiance values lower than 100 W·m^{-2}. Only LBCM, BACM and BBCM showed good performance for higher diffuse irradiance values. The errors increased significantly for South-facing sensors in all cases. This result can be explained by a higher ratio of sky-radiance anisotropy in the sky dome observed by South-facing sensors and, therefore, a greater influence of circumsolar diffuse irradiance.

Figures 8 and 9 show the distribution of the absolute residuals (differences between the corrected value and the reference) for each model with bins of 0.1 wide for k_d and $\cos\theta_{sp}$, respectively. Our graphs are quite similar to those proposed by Ineichen for the compari-

Table 7. Results for the correction models applied to several cases.

Model	MBD			RMSD			R^2		$\mu_{0.99}$		
	[W·m^{-2}]	[%]	Rank	[W·m^{-2}]	[%]	Rank	[-]	Rank	[W·m^{-2}]	[%]	Rank
North sensor											
Raw data	−11.07	14.15	7	13.71	17.53	7	0.99	7	−11.36	14.52	7
GGCM	−6.54	11.44	6	8.16	14.28	6	1.00	3	−6.82	11.93	6
BACM	0.10	0.18	2	0.70	1.25	3	1.00	5	+0.24	0.43	3
BBCM	0.01	0.02	1	0.65	1.12	2	1.00	4	+0.11	0.19	1
LBCM	0.88	1.13	3	0.56	0.72	1	1.00	1	+0.18	0.23	2
MZCM	−3.45	6.20	4	4.50	8.09	4	1.00	2	−3.88	6.97	4
STCM	−4.81	8.12	5	6.21	10.48	5	0.99	6	−5.38	9.08	5
South sensor											
Raw data	−6.89	20.96	6	12.78	38.88	6	0.98	7	−7.32	22.27	6
GGCM	1.59	8.08	4	2.81	14.28	2	1.00	2	+2.02	10.26	4
BACM	3.16	15.54	5	7.76	38.17	5	0.99	6	+4.37	21.50	5
BBCM	0.69	3.32	2	3.72	17.89	3	0.99	4	+1.46	7.02	3
LBCM	+0.28	0.86	1	2.24	6.93	1	1.00	3	−0.69	2.13	1
MZCM	−0.91	4.32	3	4.04	19.20	4	1.00	1	−1.39	6.61	2
STCM	−10.37	35.52	7	13.94	47.74	7	1.00	5	−12.21	41.82	7
East sensor											
Raw data	−10.89	42.74	7	13.99	54.91	7	0.98	7	−11.23	44.07	7
GGCM	−4.24	24.11	5	4.85	27.57	5	1.00	1	−4.70	26.72	5
BACM	+0.03	0.15	1	0.74	3.74	1	1.00	2	+0.16	0.81	1
BBCM	+0.08	0.37	2	0.74	3.39	2	1.00	3	+0.21	0.96	2
LBCM	+0.15	0.61	3	0.90	3.69	3	1.00	4	+0.29	1.19	3
MZCM	−6.31	29.21	6	7.74	35.83	6	1.00	5	−6.68	30.92	6
STCM	+1.13	5.75	4	2.38	12.12	4	1.00	6	+1.50	7.64	4
West sensor											
Raw data	−9.66	60.25	7	13.59	84.76	7	0.97	7	−10.04	62.62	7
GGCM	−3.70	34.72	5	4.86	45.60	5	1.00	2	−4.37	41.00	3
BACM	+0.23	2.22	2	1.10	10.61	1	1.00	4	+0.43	4.15	2
BBCM	+0.27	2.57	3	1.20	11.42	3	1.00	5	+0.45	4.28	4
LBCM	+0.12	0.77	1	1.17	7.55	2	1.00	6	+0.30	1.94	1
MZCM	−4.02	37.39	6	5.28	49.11	6	1.00	1	−4.46	41.48	6
STCM	−0.38	3.69	4	1.17	11.36	4	1.00	3	−0.60	5.83	5
Non-parametric aggregation											
Raw data			7 (0.001)			7 (0.001)		7 (0.001)			7 (0.001)
GGCM			6, 5 (0.001)			4 (0.001)		1 (0.001)			4 (0.001)
BACM			3 (0.001)			2, 3 (0.001)		5 (0.001)			3 (0.001)
BBCM			2, 1 (0.001)			3, 2 (0.001)		4 (0.001)			2 (0.001)
LBCM			1, 2 (0.001)			1 (0.001)		3 (0.001)			1 (0.001)
MZCM			4 (0.001)			5, 6 (0.001)		2 (0.001)			5 (0.001)
STCM			5, 6 (0.001)			6, 5 (0.001)		6 (0.001)			6 (0.001)

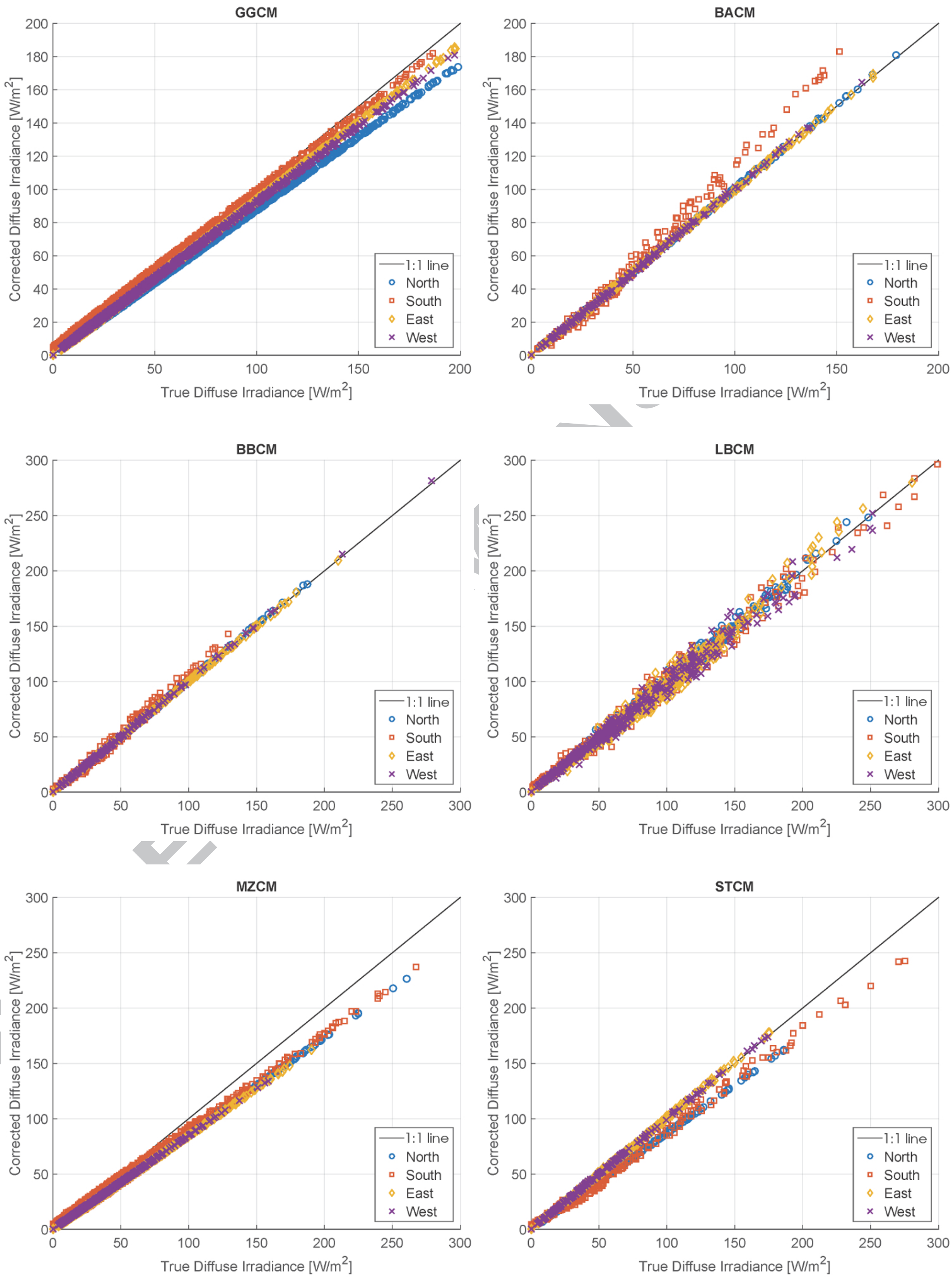

Fig. 7. Scatter plots of true diffuse values and corrected values for all models and directions considered.

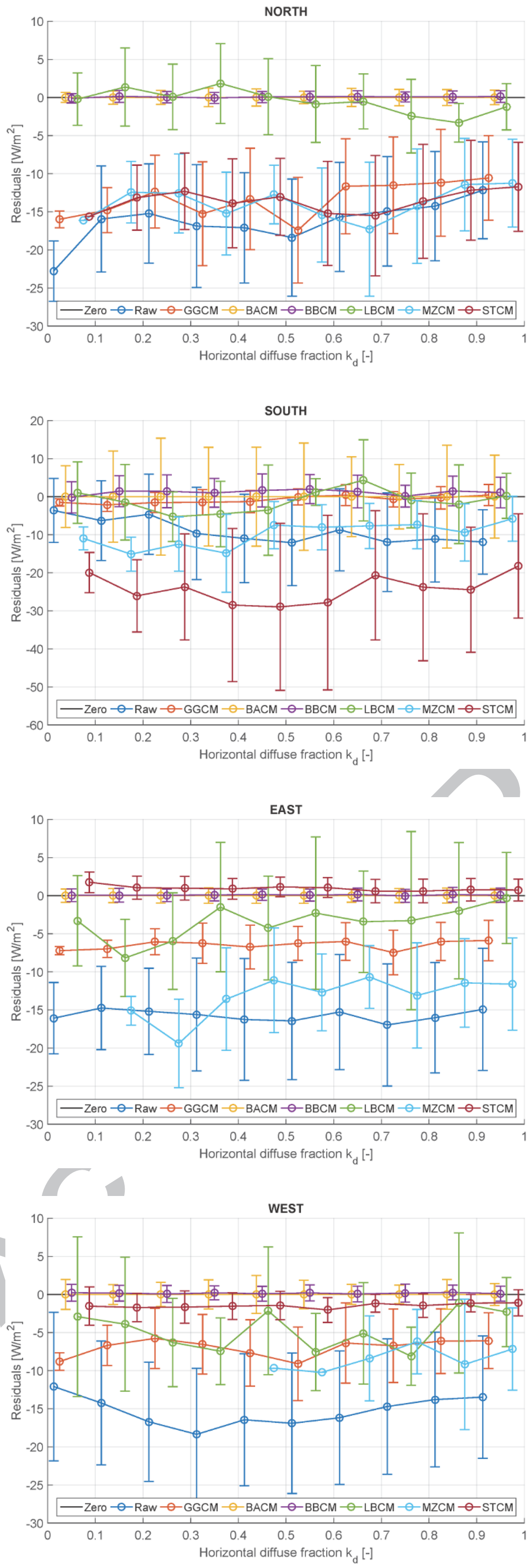

Fig. 8. Residuals of the evaluated models as a function of the horizontal diffuse fraction for each cardinal direction.

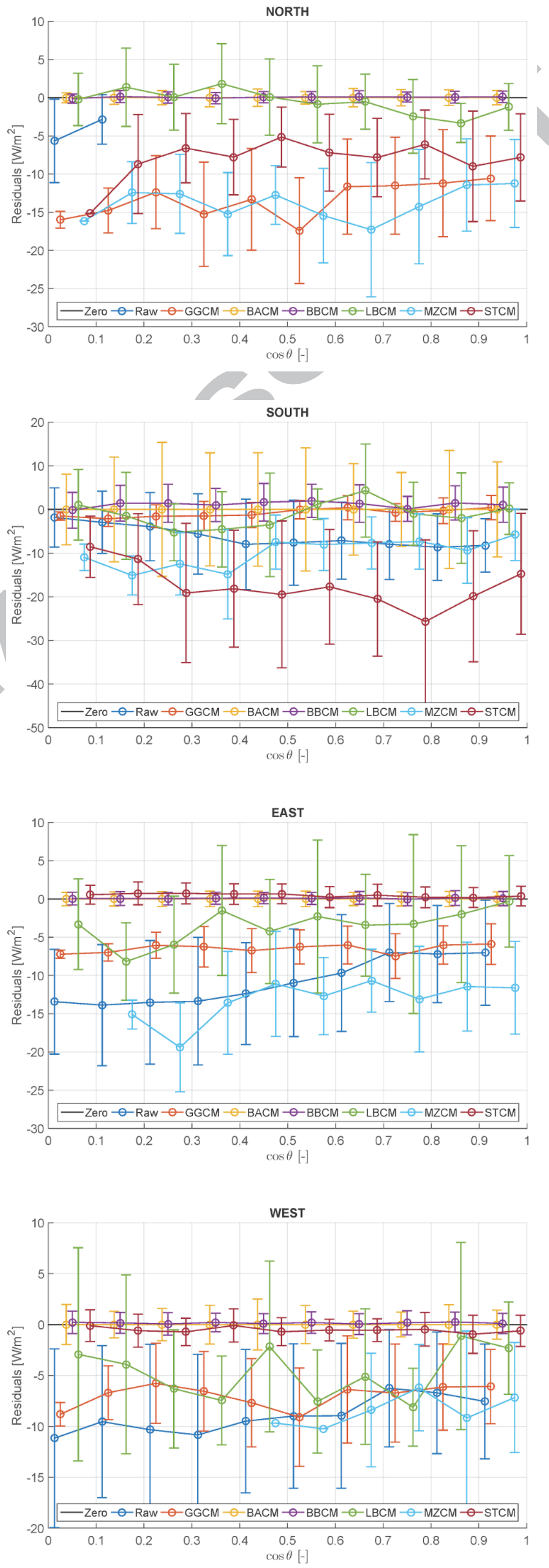

Fig. 9. As in Fig. 8, but as a function of the incident angle on the sensor.

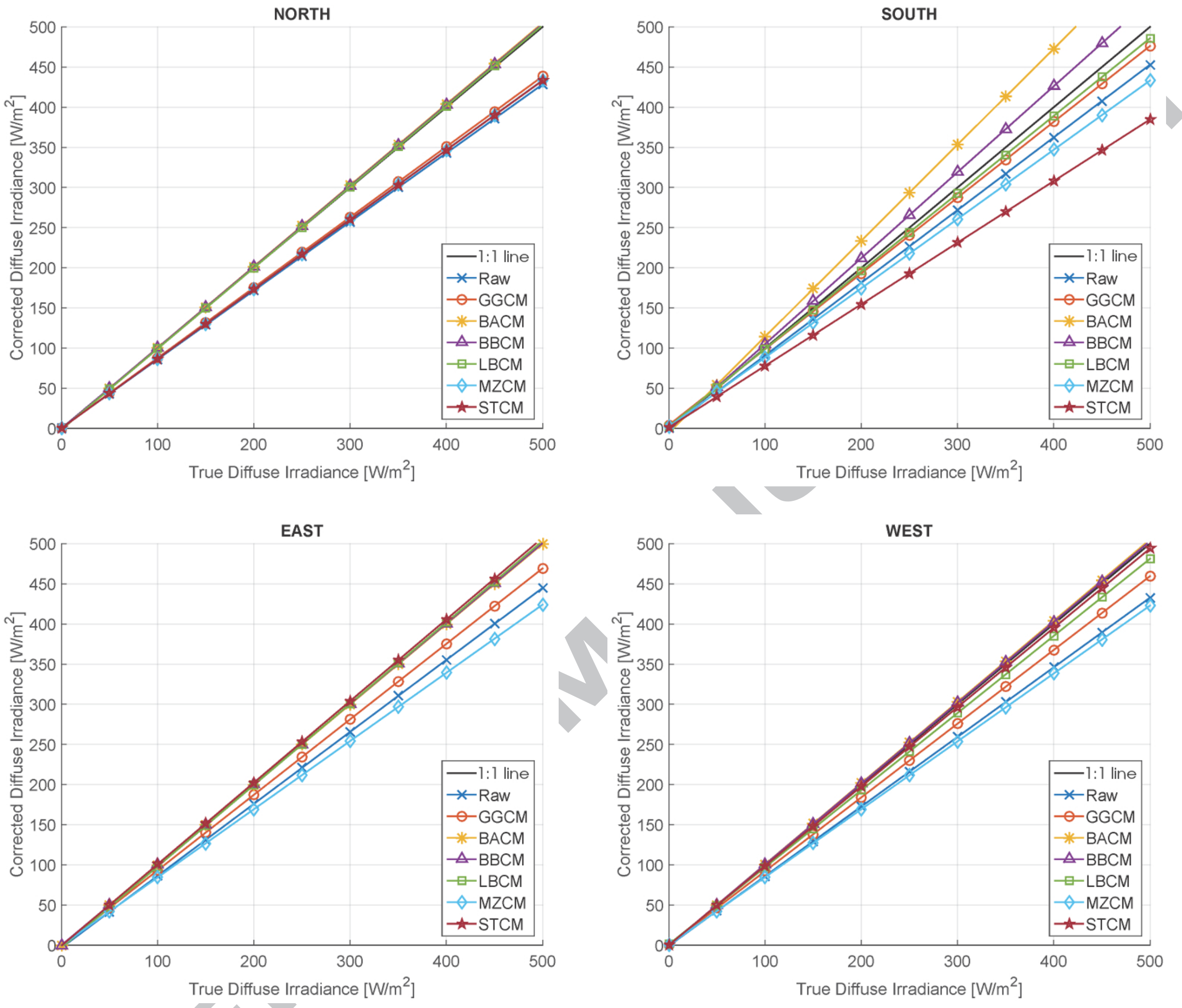

Fig. 10. Linear regression for the correlation between true diffuse values and corrected diffuse values for each cardinal direction.

son of several models against a third independent variable, preferably k_d. In this case, rather than boxplots in the interest of greater clarity, the graphs show the mean value of the absolute differences and, as error bars, the standard deviation of the residuals distribution for each bin of the horizontal k_d [defined as $k_d = D(0)/G(0)$] and $\cos\theta_{sp}$ of 0.1 width.

In both cases, results for the East- and the West-facing directions appear similar; higher values correspond to the South-facing direction. Two groups of models can be distinguished according to these criteria, specially for the North-facing direction. On the one hand, LBCM, BACM and BBCM show low mean and standard deviation values in all k_d bins. On the other hand, GGCM, MZCM and STCM show higher values for the differences. These differences have a negative sign; thus, these models tend to underestimate the vertical diffuse irradiance values. The residual distributions are quite similar in all k_d bins according to the results. The worst behavior and the highest sensitivities were observed for STCM and the South-facing direction.

No significant influence of the incident angle of beam direct irradiance ($\cos\theta_{sp}$) was observed in any case. Major variances can be observed in LBCM in this case.

Finally, in relation to Figure 10, the performance of all correction models for each cardinal direction can be seen. Both LBCM and BACM are seen to have the best performance as they have the closest results to the 1:1

line. Nevertheless, there are no great discrepancies between all models under analysis. Differences between the corrected values and the true diffuse values increase with the absolute value of true diffuse irradiance in all scenarios of the analysis. The South direction shows major discrepancies. As expected, the raw data tend to underestimate the diffuse irradiance in all cases. Moreover, GGCM, MZCM, and STCM also tend to be underestimated. There again, GACM and BBCM tend to overestimate the diffuse irradiance, specially for the South-facing direction. LBCM tends to slightly underestimate the diffuse irradiance in all cases. It was also significant that, for the East- and the West-facing directions, all models behaved in a similar way for both the East and West. In the North, GGCM and STCM tend to underestimate the diffuse irradiance values by quite a high margin.

Although other studies with vertical measurements have not been found in the relevant literature, we agree with the conclusions presented in (Batlles et al., 1995), in the sense that the simpler isotropic correction leads to high underestimation levels. The use of anisotropic models improved the diffuse irradiance corrections significantly. We also observed systematic tendencies in the distribution of differences. We found that the BACM, the BBCM, and the LBCM models stood out against the other correction models, agreeing with (Kudish and Evseev, 2008). However, we found a slightly worse performance for MZCM, maybe due to the proposed corrections for any surface given in this paper and because the authors work with hourly values while we have used ten-minute values. Finally, most of the results obtained in this paper agree with those obtained in (Sánchez et al., 2012), where correlation of all correction models for the four cardinal directions were greater than 0.9 and there were only slight variations in the residual distributions against k_d. We also found that the locally-fitted versions of the original empirical models significantly improved the estimations and our results with the models that account for irradiance anisotropy also showed remarkable improvements, in comparison with the models that only incorporated geometrical corrections (GGCM).

6. Conclusions

It can be concluded that, for the case study, any correction model improves the measures with respect to the raw data. In general terms, R^2 was always very close to 1 and MBD and RMSD values were low. The correction models greatly improved northerly-oriented measures. Furthermore, the $\mu_{0.99}$ statistical estimator appeared to be clearly representative of the model's performance and yielded really useful results to solve discrepancies between MBD and RMSD values.

According to the non-parametric aggregation procedure, LBCM obtained the best overall result and improved the accuracy of measures for MBD, RMSD and $\mu_{0.99}$ by 97%, 91%, and 96%, respectively. Moreover, GGCM improved the same statistical estimators by 60%, 62%, and 56% on average in contrast with raw data.

This study has made a positive contribution to the accurate measurement of diffuse solar irradiance in the sense that it has extended the formulae to non-horizontal surfaces and has evaluated results on vertical walls. It has, therefore, arrived at conclusions that will help improve future studies, e.g., in solar energy applications in buildings.

Acknowledgements

This research has received economic support from the Spanish Government (grant ENE2011-27511). Authors also want to acknowledge the reviewers for their valuable comments.

Appendix A. Notes on MZCM and STCM

Integrals from equations (37), (38), (40) and (41) in MZCM have complex resolution. In this work, and for the case study (vertical measurement), these expressions have been solved in an analytical way and implemented in a self-programmed MatLab routine. For the interested reader, analytical resolutions of the core integrals are presented here:

$$\begin{aligned}
&\int_{\omega_1}^{\omega_2} \frac{1+b\cos\theta_{zr}}{1+b}\cos\xi_{shp}d\omega = \frac{1}{1+b}A'\left(\omega_2-\omega_1\right)\\
&+\frac{1}{1+b}\left[B'\left(\sin\omega_2-\sin\omega_1\right)-C'\left(\cos\omega_2-\cos\omega_1\right)\right]\\
&+\frac{b}{1+b}\left[A'D'\left(\omega_2-\omega_1\right)+\left(B'D'+A'E'\right)\left(\sin\omega_2-\sin\omega_1\right)\right]\\
&+\frac{b}{1+b}\left[\frac{C'E'}{2}\left(\cos^2\omega_2-\cos^2\omega_1\right)-C'D'\left(\cos\omega_2-\cos\omega_1\right)\right]\\
&+\frac{b}{1+b}\frac{B'E'}{2}\left[\frac{\sin\left(2\omega_2\right)}{2}+\omega_2-\frac{\sin\left(2\omega_1\right)}{2}-\omega_1\right],
\end{aligned} \tag{A.1}$$

where constants A', B', C', D' and E' are defined in the following expressions:

$$A' = \sin\delta_s \sin\phi_g \cos\theta_{zp} - \sin\delta_s \cos\phi_g \sin\theta_{zp} \cos\gamma_p. \quad (A.2)$$

$$B' = \cos\delta_s \cos\phi_g \cos\theta_{zp} + \cos\delta_s \sin\phi_g \sin\theta_{zp} \cos\gamma_p. \quad (A.3)$$

$$C' = \cos\delta_s \sin\theta_{zp} \sin\gamma_p. \quad (A.4)$$

$$D' = \sin\delta_s \sin\phi_g. \quad (A.5)$$

$$E' = \cos\delta_s \cos\phi_g. \quad (A.6)$$

In above expressions, δ_s and ϕ_g are the Sun's declination and the geographical latitude, respectively.

$$\int_{\gamma_1}^{\gamma_2} \int_0^{\pi/2} \frac{1 + b\cos\theta}{1+b} \cos\xi_p \sin\theta d\theta d\gamma = \frac{1}{1+b}\left(\frac{\pi}{4} + \frac{b}{3}\right)\left[\sin\left(\gamma_2 - \gamma_p\right) - \sin\left(\gamma_1 - \gamma_p\right)\right]. \quad (A.7)$$

Similiarly, the analytical resolution of the core integral in equation (45) from STCM is showed here:

$$\int_{\omega_1}^{\omega_2} \cos\theta_{sp} d\omega = A'(\omega_2 - \omega_1) + B'(\sin\omega_2 - \sin\omega_1) - C'(\cos\omega_2 - \cos\omega_1). \quad (A.8)$$

References

Batlles, F. J., Olmo, F. J., Alados-Arboledas, L., Feb. 1995. On shadowband correction methods for diffuse irradiance measurements. Solar Energy 54 (2), 105–114.

de Miguel, A., Bilbao, J., Aguiar, R., Kambezidis, H., Negro, E., 2001. Diffuse solar irradiation model evaluation in the North Mediterranean Belt area. Solar Energy 70 (2), 143–153.

de Simón-Martín, M., Alonso-Tristán, C., González-Peña, D., Díez-Mediavilla, M., Sep. 2015. New device for the simultaneous measurement of diffuse solar irradiance on several azimuth and tilting angles. Solar Energy 119, 370–382.

Drummond, A. J., Sep. 1956. On the measurement of sky radiation. Archiv für Meteorologie, Geophysik und Bioklimatologie, Serie B 7 (3-4), 413–436.

Drummond, A. J., 1964. Comments on “sky radiation measurement and corrections”. Journal of Applied Meteorology 3 (6), 810–811.

Ineichen, P., Gremaud, J. M., Guisan, O., Mermoud, A., 1983. Study of the corrective factor involved when measuring the diffuse solar radiation by use of the ring method. Solar Energy 31 (1), 113–117.

Joint Committee for Guides in Metrology, 2008. Evaluation of measurement data: Guide to the expression of uncertainty in measurement. GUM 1995 with minor revisions. Bureau International des Poids et Mesures.

Kipp and Zonen, 2014. CM 121 shadow ring instruction manual.

Kudish, A. I., Evseev, E. G., Feb. 2008. The assessment of four different correction models applied to the diffuse radiation measured with a shadow ring using global and normal beam radiation measurements for Beer Sheva, Israel. Solar Energy 82 (2), 144–156.

LeBaron, B. A., Michalsky, J. J., Perez, R., 1990. A simple procedure for correcting shadowband data for all sky conditions. Solar Energy 44 (5), 249–256.

López, G., Muneer, T., Claywell, R., 2004. Assessment of four shadow band correction models using beam normal irradiance data from the United Kingdom and Israel. Energy Conversion and Management 45 (13-14), 1963–1979.

Moore, D., McCabe, G., 2000. Introduction to the Practice of Statistics, 3rd Edition. Vol. 1. W.H. Freeman and Company, New York.

Muneer, T., 2004. Solar Radiation and Daylight Models, 2nd Edition. Vol. 1. ButterWorth-Heinemann, Oxford.

Muneer, T., Zhang, X., 2002. A new method for correcting shadow band diffuse irradiance data. Journal of Solar Energy Engineering, Transactions of the ASME 124 (1), 34–43.

Perez, R., Ineichen, P., Seals, R., Michalsky, J., Stewart, R., 1990. Modeling daylight availability and irradiance components from direct and global irradiance. Solar Energy 44 (5), 271–289.

Perez, R., Seals, R., Ineichen, P., Stewart, R., Menicucci, D., 1987. A new simplified version of the perez diffuse irradiance model for tilted surfaces. Solar Energy 39 (3), 221–231.

Sánchez, G., Serrano, A., Cancillo, M., 2013. Shadow-band correction for diffuse ultraviolet radiation measurements. Journal of Geophysical Research D: Atmospheres 118 (9), 3807–3816.

Sánchez, G., Serrano, A., Cancillo, M. L., García, J. A., May 2012. Comparison of shadow-ring correction models for diffuse solar irradiance. Journal of Geophysical Research: Atmospheres 117 (D9), D09206.

Sengupta, M., Habte, A., Kurtz, S., Dobos, A., Wilbert, S., Lorenz, E., Stoffel, T., Renné, D., Gueymard, C., Myers, D. R., Wilcox, S., Blanc, P., Perez, R., 2015. Best practices handbook for the collection and use of solar resource data for solar energy applications.

Steven, M., Unsworth, M., 1980. Shade ring corrections for pyranometer measurements of diffuse solar radiation from cloudless skies. Quarterly Journal, Royal Meteorological Society 106 (450), 865–872.

Steven, M. D., 1984. The anisotropy of diffuse solar radiation determined from shade-ring measurements. Quarterly Journal of the Royal Meteorological Society 110 (463), 261–270.

Stone, R. J., Oct. 1993. Improved statistical procedure for the evaluation of solar radiation estimation models. Solar Energy 51 (4), 289–291.

Stone, R. J., Jul. 1994. A nonparametric statistical procedure for ranking the overall performance of solar radiation models at multiple locations. Energy 19 (7), 765–769.

WMO, 2010. Guide to Meteorological Instruments and Methods of Observation, 2010th Edition. Vol. 1 of WMO. WMO.

Yang, D., Oct. 2016. Solar radiation on inclined surfaces: Corrections and benchmarks. Solar Energy 136, 288–302.

Highlights for "Shadow-band radiometer measurement of diffuse solar irradiance: calculation of geometrical and total correction factors"

- A generalized expression for the geometrical correction for shadow-bands is proposed.
- Total correction models have been reformulated to be used on any measurement plane.
- A new statistical estimator for models' performance analysis is proposed: $\mu_{1-\alpha}$.
- 10-min measurements and models' estimations on 4 vertical planes have been compared.
- Models have been studied against the diffuse fraction and the Sun's incidence angle.
- Results can be extended to any shadow-band radiometer system.